Trajectory estimation with GNSS, IMU and LiDAR for terrestrial/kinematic laser scanning

Florian Pöppl[a⋆], Martin Pfennigbauer[b], Andreas Ullrich[b], and Norbert Pfeifer[a]

[a]Technische Universität Wien, Wiedner Hauptstraße 8, Vienna, Austria
[b]RIEGL Laser Measurement Systems GmbH, Riedenburgstrasse 48, 3580 Horn, Austria

ABSTRACT

Kinematic laser scanning allows for efficient acquisition of large-scale and highly accurate 3D data. Georeferencing of the LiDAR data requires integration with auxiliary navigation systems. The standard processing pipeline consists of GNSS/IMU integration, georeferencing, and subsequent adjustment of the laser data. In contrast, we propose a holistic approach for GNSS, IMU and LiDAR integration where all measurements are incorporated in a single model, thereby enabling accurate estimation of both trajectory and system calibration parameters. This method is applied to the case of a 3D laser scanner mounted on a moving platform. We demonstrate precise georeferencing of the kinematically acquired data by comparison to statically acquired reference data.

Keywords: Kinematic mapping, sensor fusion, sensor orientation, in-run calibration.

1. INTRODUCTION

Laser scanning is a surveying technique which enables large-scale acquisition of highly accurate and spatially dense 3D data, specifically point clouds. Laser scanning uses light detection and ranging (LiDAR) together with a scanning mechanism to achieve 3D coverage of the surroundings. An important distinction is between terrestrial laser scanning (TLS), where the laser scanner is stationary during data acquisition and kinematic laser scanning (KLS), where the laser scanner is moving during data acquisition. For TLS, the limiting factor for the accuracy of the final point cloud is the laser ranging accuracy and the scan mechanism's angular accuracy. For KLS, this is usually significantly overshadowed by the (limited) accuracy of the laser scanner's position and orientation: Kinematic laser scanning requires knowledge of the scanner trajectory (position and orientation over time) to allow for transformation of the laser measurements from the scanner's coordinate system to a georeferenced coordinate system. This is achieved by integrating navigation sensors, specifically an inertial measurement unit (IMU) and a global navigation satellite system (GNSS). Data from IMU and GNSS are commonly fused via Kalman filter, and the resulting trajectory is used for the georeferencing of the laser data. However, errors in this trajectory propagate through the georeferencing process and result in errors in the measured 3D data, i.e., point cloud[1]. It is possible to correct for such errors at the trajectory level to ensure consistent point clouds. This is done in an adjustment step subsequent to GNSS/IMU processing by minimizing discrepancies between overlapping point clouds[2]. For further details on trajectory estimation in the context of kinematic laser scanning, refer to the authors recent survey paper Ref. 3.

In contrast to the aforementioned two-stage process, we propose a holistic method for integrating GNSS, IMU and LiDAR data based on simultaneous adjustment of all measurement data to obtain an accurate trajectory and thus point cloud. The underlying methodology was recently presented in the context of airborne laser scanning[4] and is adapted here to mobile mapping. Incorporating all available data allows for rigorous sensor-level error modelling, which in turn enables more reliable estimation of the deterministic or time-correlated error components of the inertial sensors (e.g., accelerometer and gyroscope bias). As a consequence, even low-cost inertial sensors may be used while retaining a high accuracy of the final data. The development of this holistic sensor integration method presented here allows the *RIEGL* VZ-600i (Fig. 1), a terrestrial laser scanner, to be used kinematically for mobile laser scanning (MLS) using the onboard navigation sensors (Fig. 2): The VZ-600i comprises an RTK-GNSS receiver and antenna for positioning and an IMU for short-term relative orientation.

⋆florian.poeppl@geo.tuwien.ac.at; photo.geo.tuwien.ac.at

Citation: Florian Pöppl, Martin Pfennigbauer, Andreas Ullrich, and Norbert Pfeifer "Trajectory estimation with GNSS, IMU, and LiDAR for terrestrial/kinematic laser scanning", Proc. SPIE 12537, Laser Radar Technology and Applications XXVIII, 1253706 (12 June 2023); https://doi.org/10.1117/12.2663454.

Figure 1: *RIEGL* VZ-600i terrestrial laser scanner with onboard IMU and RTK-GNSS.

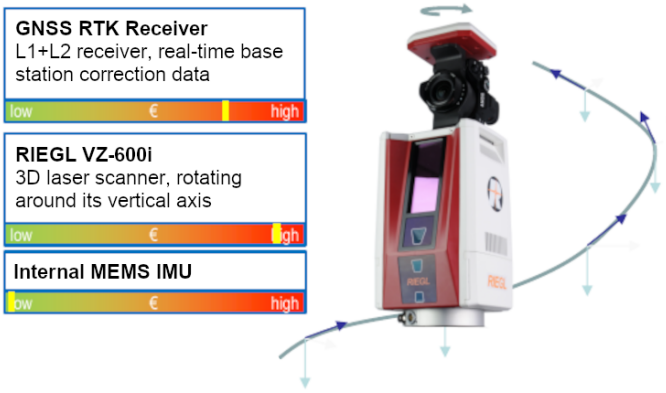

Figure 2: Kinematic mapping possible by using the built-in survey-grade GNSS and low-cost IMU.

While the achieved accuracy and precision in kinematic mode remains less than that of static acquisitions, we demonstrate sufficiently high accuracy and precision, with lower acquisition times. Additionally, the kinematic scan data may be used to improve stop-and-go acquisitions by densifying the point cloud in-between static scans.

The rest of this paper is organized as follows: In Section 2 we present the sensor fusion methodology. In Section 3, we demonstrate the method by comparison to terrestrially acquired reference data. In Section 4, we summarize the results and discuss possible future work.

2. TRAJECTORY ESTIMATION AND SENSOR CALIBRATION

The presented method is a holistic sensor integration methodology based on batch non-linear least-squares (NLS) estimation. It estimates all relevant parameters in a single estimation procedure and considers the GNSS position data, IMU acceleration and angular velocity measurements, and observations derived from the LiDAR point cloud simultaneously. The statistical framework is that of maximum a-posteriori (MAP) estimation, an approach which is also widespread in the robotics community (e.g., in the context of SLAM[5]).

Consider a set of n noisy vector-valued measurements $\widetilde{\boldsymbol{y}}_i$ of true values $\boldsymbol{y}_i$. We model these measurements as a function of unknown parameters $\boldsymbol{x}$, so that

$$\boldsymbol{y}_i := f_i(\boldsymbol{x}), \quad \text{and} \quad \widetilde{\boldsymbol{y}}_i := f_i(\boldsymbol{x}) + \boldsymbol{\epsilon}_i, \tag{2.1}$$

where $\boldsymbol{\epsilon}_i$ is Gaussian noise with variance $\boldsymbol{\Sigma}_i$. The measurement noise $\boldsymbol{\epsilon}_i$ is assumed to be pairwise uncorrelated. Additionally assuming a Gaussian prior for some (or all) of the parameters, the MAP estimator for $\boldsymbol{x}$ is equivalent to the NLS estimator and given by

$$\boldsymbol{x}^* = \underset{\boldsymbol{x}}{\operatorname{argmin}} \sum_i (f_i(\boldsymbol{x}) - \widetilde{\boldsymbol{y}}_i)^T \boldsymbol{\Sigma}_i^{-1} (f_i(\boldsymbol{x}) - \widetilde{\boldsymbol{y}}_i). \tag{2.2}$$

This is a minimization problem which may be solved by standard non-linear optimization techniques, in this case using the Levenberg-Marquardt algorithm. In the following, we briefly describe the details of the employed models, specifically:

- the parameters $\boldsymbol{x}$,
- the functional model, described by $\boldsymbol{x} \mapsto f_i(\boldsymbol{x})$,
- the stochastic model, described by $\widetilde{\boldsymbol{y}} = \boldsymbol{y} + \boldsymbol{\epsilon}_i,\ \boldsymbol{\epsilon}_i \sim N(\boldsymbol{0}, \boldsymbol{\Sigma}_i)$.

Model parameters

All sensors considered here are mounted rigidly on a moving platform. The estimable quantities in this sensor fusion problem are then made up of three types: the trajectory of the platform itself, system calibration parameters and certain object space parameters.

- **Trajectory:** The trajectory describes the scanner's position and orientation over time. To achieve a high-quality point cloud, the trajectory needs to be known with a sufficiently high frequency and fidelity. Here, we model the position using cubic Euclidean B-splines and the orientation using quadratic quaternion B-splines[6]. Spline nodes are set at the frequency of the IMU measurements to allow representation of high-frequency dynamics. For ease of presentation, we consider the platform coordinate frame and IMU coordinate frame to be identical.
- **Calibration:** Fusing measurements from the different sensors requires knowledge of the relative geometric relation between them, in this case: the position and orientation of the scanner, and the position of the GNSS antenna, both relative to the IMU. Given sufficiently close starting values, these parameters can be estimated together with the trajectory. This is not the focus here however, as the factory calibration has proven to be suitably accurate. Note that while the scanner rotates around its base, all components (scanning mechanism and laser origin, inertial sensors and GNSS receiver/antenna) are located on the rotating part. The aforementioned calibration parameters are assumed to stay constant over longer periods and when power cycling the device. The inertial sensors additionally exhibit errors which change from run to run, and also vary over time within each run. These errors may be calibrated in-run, given a suitable model for their behavior is known[7].
- **Objects**: The final component is a model of the physical space (the object space) as measured by the laser scanner. Here, we restrict ourselves to planar surfaces which are extracted from the point clouds. Each planar object is modelled by three parameters: an offset and two tilts, with respect to its initial position and orientation (see also Eq. (2.5)). These object space model parameters are optimized jointly together with the other parameters.

Measurement models

GNSS measurement model

In this work, we use an RTK-GNSS-based integration architecture. The GNSS position measurements are computed in real-time on the device using correction data from a nearby base station. For a time t, the measurement equation of a GNSS position measurement $\widetilde{\boldsymbol{p}}$ is given by

$$\underbrace{\widetilde{\boldsymbol{p}}}_{\text{measurement}} = \underbrace{\boldsymbol{p}(t) + \boldsymbol{R}(t)\,\boldsymbol{l}_g}_{\text{model}} + \underbrace{\boldsymbol{\epsilon}_p}_{\text{noise}}, \tag{2.3}$$

where $\boldsymbol{p}(t)$ is the platform position, $\boldsymbol{R}(t)$ the platform orientation and $\boldsymbol{l}_g$ the (known or estimable) position of the GNSS antenna in the platform frame. The measurement error $\boldsymbol{\epsilon}_p$ is assumed zero-mean and normally distributed with covariance $\boldsymbol{\Sigma}_p$, of which an estimate is available from the RTK-GNSS processing.

IMU measurement model

The accelerometer and gyroscope provide high frequency* measurements $\widetilde{\boldsymbol{f}}, \widetilde{\boldsymbol{\omega}}$ of specific force $\boldsymbol{f}$ and angular velocity $\boldsymbol{\omega}$. The measured values are tainted by additive white noise $\boldsymbol{\epsilon}_\star$, biases $\boldsymbol{b}_\star$ and scale factors $\boldsymbol{S}_\star = \operatorname{diag}(s_{x\star}, s_{y\star}, s_{z\star})$. The measurement model for specific force and angular velocity at time t is thus given by

$$\underbrace{\begin{matrix}\widetilde{\boldsymbol{f}} \\ \widetilde{\boldsymbol{\omega}}\end{matrix}}_{\text{measurement}} = \underbrace{\begin{matrix}(1+\boldsymbol{S_f})\,\boldsymbol{f}(t) + \boldsymbol{b}_f(t) \\ (1+\boldsymbol{S_\omega})\,\boldsymbol{\omega}(t) + \boldsymbol{b}_\omega(t)\end{matrix}}_{\text{model}} + \underbrace{\begin{matrix}\boldsymbol{\epsilon}_f \\ \boldsymbol{\epsilon}_\omega\end{matrix}}_{\text{noise}} \tag{2.4}$$

*The IMU used here outputs measurements with 400 Hz, which is high in comparison to the 7 Hz output rate of the RTK-GNSS positions. The IMU is usually the sensor responsible for capturing the higher frequency trajectory dynamics.

The modelled values for $\boldsymbol{f}$ and $\boldsymbol{\omega}$ are derived from platform position and orientation using the strap-down inertial navigation equations (for details see Refs. 3 and 8).

The biases, scale factors and the noise are stochastic processes with certain characteristics. These process characteristics may be obtained in a static calibration using Allan variance analysis (see Ref. 7). This is done here for the white noise processes $\boldsymbol{\epsilon}_\star$ and the biases $\boldsymbol{b}_\star$; the latter are modelled as random walk processes. The scale factors $\boldsymbol{S}_\star$ are kept constant throughout the data acquisition (i.e., until the device is turned off again).

LiDAR measurement model

The LiDAR measurements are based on the assumptions that repeatedly observed objects in physical space remain stationary and as such may be used to constrain the trajectory. Specifically, we extract planar surfaces from point clouds, and segment planar surfaces by their acquisition time. In Ref. 4, we employed a simple method for feature extraction based on voxelization and principal component analysis (PCA). This is effective in airborne laser scanning and generally in use cases with large-scale topological features. Here, we use a robust and adaptive method based on Ref. 9 in conjunction with PCA, in order to extract both large features (e.g., facades) as well as small features (e.g., sidewalk curbs). While the extraction method used here is more suitable to the application (ground-based mobile mapping), the rest of the measurement model remains the same as in Ref. 4.

Each planar feature is an aggregation of multiple laser points. It is described by a plane center $\widetilde{\boldsymbol{c}}$ and plane normal $\widetilde{\boldsymbol{n}}$. Multiple planar features may correspond to the same physical plane (cf. Fig. 3), which is also described by a plane center $\boldsymbol{c}$ and plane normal $\boldsymbol{n}$. Assuming these planar features describe the same object, we impose the constraint that all feature planes coincide with their object plane in terms of normal distance and distance between their axes

$$\underbrace{\begin{aligned} \mathbf{0} &= ((\boldsymbol{c} - \widetilde{\boldsymbol{c}}) \cdot \boldsymbol{n}) \\ \mathbf{0} &= (\widetilde{\boldsymbol{n}} \cdot \boldsymbol{k}_1) \\ \mathbf{0} &= (\widetilde{\boldsymbol{n}} \cdot \boldsymbol{k}_2) \end{aligned}}_{\text{constraint}} + \underbrace{\begin{aligned} \boldsymbol{\epsilon}_n \\ \boldsymbol{\epsilon}_{k_1} \\ \boldsymbol{\epsilon}_{k_2} \end{aligned}}_{\text{noise}} \tag{2.5}$$

Here, $\boldsymbol{k}_1, \boldsymbol{k}_2$ and $\widetilde{\boldsymbol{k}}_1, \boldsymbol{k}_2$ are axes of the feature and object plane and are arbitrarily chosen so that $(\widetilde{\boldsymbol{k}}_1, \widetilde{\boldsymbol{k}}_2, \widetilde{\boldsymbol{n}})$ and $(\boldsymbol{k}_1, \boldsymbol{k}_2, \boldsymbol{n})$ are orthonormal. Each feature plane is internally stored as center $\widetilde{\boldsymbol{c}}_s$ and normal $\widetilde{\boldsymbol{n}}_s$ in the scanner coordinates, and is transformed into physical coordinates using the georeferencing equation

$$\begin{aligned} \widetilde{\boldsymbol{c}} &= \boldsymbol{R}(t)\, \boldsymbol{M}_s\, (\widetilde{\boldsymbol{c}}_s + \boldsymbol{l}_s) + \boldsymbol{p}(t), \\ \widetilde{\boldsymbol{n}} &= \boldsymbol{R}(t)\, \boldsymbol{M}_s\, \widetilde{\boldsymbol{n}}_s, \end{aligned} \tag{2.6}$$

where $\boldsymbol{M}_s$ and $\boldsymbol{l}_s$ describe the orientation and position of the scanner with respect to the IMU. The random errors occurring in Eq. (2.5) are assumed to be uncorrelated and Gaussian, with covariances derived from the PCA results, taking into account the angle of incidence and the laser footprint.

Full processing workflow

The non-linear estimation described above forms the core of the proposed method. However, some additional steps are necessary in order to a) obtain suitable initial values for the non-linear optimization subproblem and b) extract the planar features from the point cloud. The full processing workflow is depicted in Fig. 4 and can be summarized as follows:

1. On-board RTK-GNSS processing,
2. Kalman filtering of GNSS positions and IMU measurements to obtain an initial trajectory,
3. non-linear least-squares trajectory estimation using GNSS and IMU data,
4. georeferencing with GNSS/IMU trajectory to obtain an initial point cloud,
5. extracting planar features and objects to build LiDAR correspondences,
6. non-linear least-squares trajectory estimation using GNSS, IMU and LiDAR data,
7. georeferencing with GNSS/IMU/LiDAR trajectory to obtain the final point cloud.

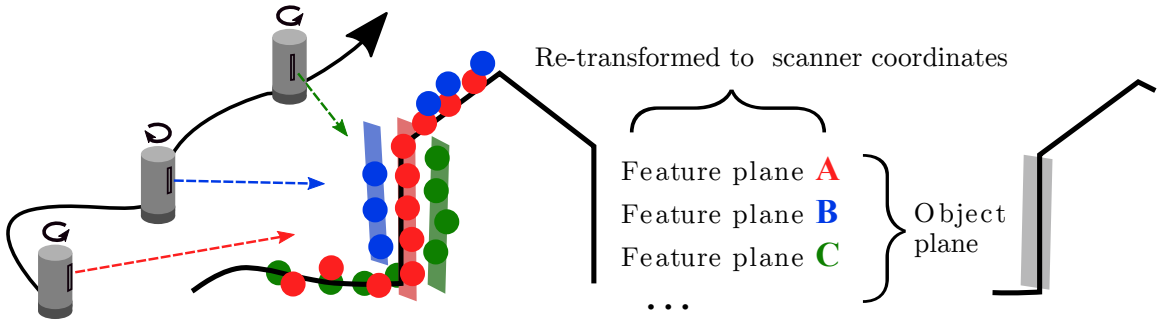

Figure 3: Due to the rotation of the scanner, objects are scanned multiple times from different positions. *Feature planes* are extracted separately from points belonging to different rotations, and the corresponding feature planes are then matched to a single *object plane*.

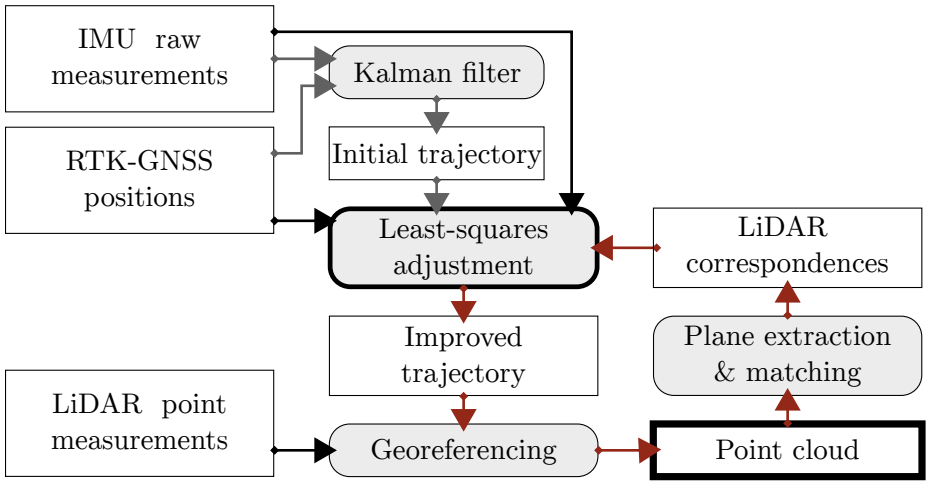

Figure 4: Proposed kinematic LiDAR mapping workflow.

Steps 4.-7. may optionally be iterated if the initial trajectory or system calibration is insufficiently accurate to obtain enough LiDAR correspondences. This is not done here, as the IMU-to-LiDAR mounting parameters are accurately known.

Scanner frame rotation

A 3D terrestrial laser scanner used for mobile laser scanning (MLS) exhibits one obvious difference compared to other MLS systems: It rotates around its vertical axis (cf. Fig. 2). Most survey-grade MLS systems are 2D laser scanners which obtain 3D coverage through the motion of the carrier platform[1]. This inherent 3D nature of a terrestrial laser scanner used kinematically has two benefits: For one, it reduces scan shadows caused by occlusions (Fig. 6). Also, usage of alternating rotation patterns helps improve in-run calibration of the inertial sensors and allows for straightforward temporal calibration of the IMU-LiDAR system.

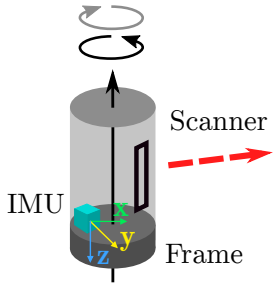

Figure 5: Scanner frame rotation.

In any sensor fusion task, it is critical that the measurements of the different sensors are accurately timestamped. The source of truth for timing is the GNSS, which provides highly accurate timing signals (PPS signal) to all other components. The time synchronization between GNSS, laser scanner and the angular encoder of the

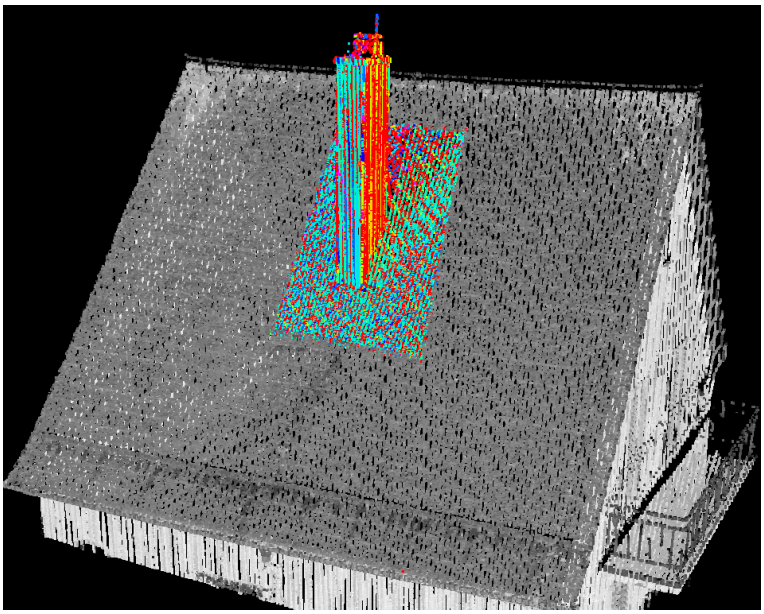

Figure 6: Rooftop with chimney. The roof is repeatedly scanned at different times and from different angles due to the frame rotation. Front, left and right sides of the chimney as well as the area behind the chimney are fully scanned. Points near the chimney are colored by their acquisition time (cf. Fig. 3).

rotating frame is already sufficiently precise, but this is not the case for the IMU. Initial experiments have shown a significant impact of even small delays in the inertial measurements on the final trajectory. The MEMS IMU used here outputs measurements with 400 Hz, but samples faster internally. The high frequency samples are low-pass filtered and decimated. The exact workings of the internal filtering and decimation are unknown to the user, but cause a time delay between the measurement timestamps and the corresponding physical measurement times. By treating the rotating frame of the scanner (cf. Fig. 5) as an ad-hoc single-axis rotary table, time synchronization between IMU and laser scanner and partial calibration of IMU turn-on errors may be achieved by a calibration procedure similar to the strapdown rotation test[10].

During scan data acquisition, an alternating rotation pattern is used. The scanner rotates with a given speed for a specified duration and then switches the direction of rotation. In the experiments presented below, the rotation speed is $\pm 150\,\mathrm{deg/s}$, reversing direction every 15 s. The changing of direction is beneficial for estimating the bias and scale factors of the gyroscope z-axis. With a constant but very high rotational speed, a bias and a scale factor would have a similar effect and thus correlate highly. By alternatingly changing the direction of rotation, these effects of bias and scale factor may be separated, improving the in-run calibration of the gyroscope z-axis. This has a large effect on the trajectory quality, as the gyroscope z-axis is the main sensor responsible for resolving short-term changes in the yaw angle of the platform.

3. CASE STUDIES IN TERRESTRIAL/KINEMATIC MAPPING

The proposed methodology is demonstrated by comparing kinematic data acquisitions to terrestrially (statically) acquired reference data. The study area is an approximately 200 m x 300 m large block in a residential area in Horn, Lower Austria. The terrestrial reference data is acquired with the same *RIEGL* VZ-600i laser scanner from 100 static scan positions, resulting in a point cloud consisting of over 1.8 billion points. The distribution of the individual static scan positions is shown in Fig. 7. Data acquisition was performed in two clockwise circles, starting and ending at the northern street corner. A scan is done every 10 meters, each taking approximately 1 minute, with a total duration of 105 minutes. Fig. 8 and Fig. 9 show scan positions overlaid over the point cloud. All scan positions are co-registered together, without additional control points. Repeated, independent data acquisitions over the course of two weeks differ at most 1 cm in height and even less in planimetry. The

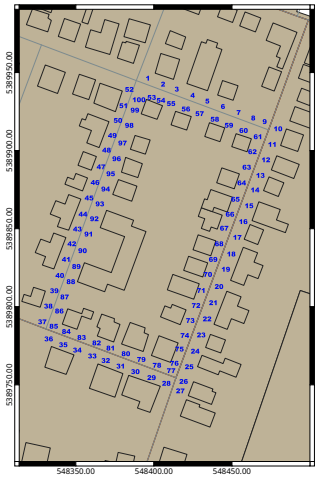

Figure 7: Study area with 100 TLS scan positions.

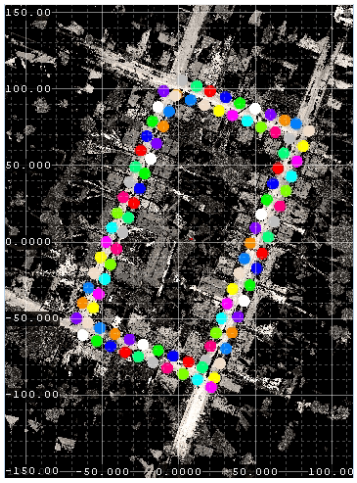

Figure 8: Pointcloud colored by reflectance, top-down view.

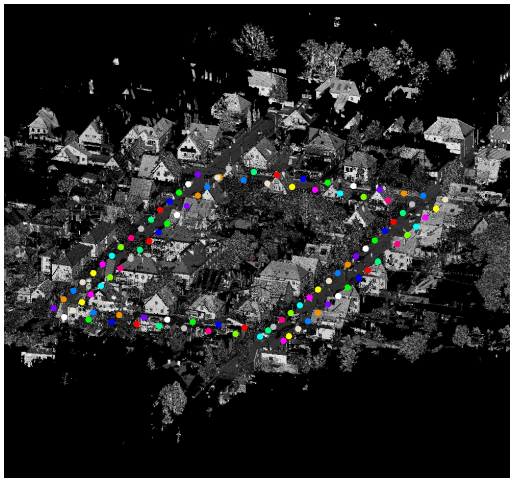

Figure 9: Pointcloud colored by reflectance, side-view.

TLS data is thus assumed to be accurate enough to serve as comparison for the kinematic data, at least at the centimeter-level. For the kinematic data acquisitions, three different system setups are used:

1. Laser scanner mounted on the roof rack of a car (Fig. 10a).
2. Laser scanner mounted on a cargo bike (Fig. 10b).
3. Laser scanner carried on foot using a backpack frame (Fig. 10c).

The *car* datset consists of two passes (clockwise and counter-clockwise) around the study area and the neighboring block. Data acquisition took a total of 7 minutes, resulting in a point cloud with 160 million points (Fig. 11a). The *bike* dataset consists of two passes (clockwise and counter-clockwise) around the study area. Data acquisition took a total of 8 minutes, resulting in a point cloud with 200 million points (Fig. 11b). The *on-foot* dataset consists of one clockwise pass around the study area. Data acquisition took a total of 6 minutes, resulting in a point cloud with 115 million points (Fig. 11c).

In order to compare the accuracy of the proposed method in conjunction with the three system setups, the kinematic point clouds are compared to the reference point cloud. Specifically, we compute a voxelization for the reference point cloud with 0.25 m voxel size and perform a principal component analysis (PCA) of all points in each voxel. From the PCA results a best-fit plane for all voxels with a minimum of 16 points is derived. Then,

(a) VZ-600i on car roof.

(b) VZ-600i on cargo bike.

(c) VZ-600i on backpack.

Figure 10: Three different setups for kinematic data acquisition with a *RIEGL* VZ-600i.

for each point in the kinematic point clouds, the points normal distance to the nearest voxels' best-fit plane is computed. If a point is more than 0.25 m away from a reference voxel, it is not considered for comparison. The results of this analysis for the car, bike and on-foot point clouds are shown in Fig. 12a, Fig. 12b and Fig. 12c, respectively. The overall fit with respect to the TLS reference data is good, with maximum differences of 2.5 cm for planar reference surfaces in all three datasets. Large difference values appear only on non-planar objects, such as wire fences or vegetation. Still, there are some systematic differences on the order of 1-2 cm visible in all three datasets. These may be caused by errors in the RTK-GNSS solution, e.g. due to occlusions and multi-path effects. Additionally, our reference data may not be perfectly accurate, as discussed above.

Quantitative evaluation of the results is not straightforward, due to the difficulty with differentiating actual errors from discrepancies due to differing viewpoints, moving objects or vegetation. Still, we use the point-to-reference-surface distance as an error measure and aim for a simplistic evaluation procedure, presenting the statistics for distances both for the full data as well as for robust subsets of the data. The robust versions of the statistics are obtained by cutting off the 2.5 (resp. 97.5), and 5.0 (resp. 95.0) percentiles with respect to the point-to-reference distances. Table 1 shows the minimum (MIN), root mean square error (RMSE), and maximum (MAX) of the point-to-reference distances for the full dataset and the robustified versions thereof.

For the full dataset, the minimum and maximum values are by definition smaller than ±0.25 m due to the maximum search radius of one voxel size (= 0.25 m) during comparison. The standard deviation of ∼3 cm is larger than what would be expected from Figs. 12a–12c, because spurious distances from e.g. vegetation points are included in this measure. The robustified statistics are more optimistic and arguably more realistic: with the top and bottom 5% cut off, the minimum and maximum errors of ±3 cm to ±5 cm, are more in line with a qualitative assessment of Figs. 12a–12c. The distances between kinematic data and terrestrial data have a RMSE which is certainly less than 3.6 cm, and optimistically below 1.5 cm.

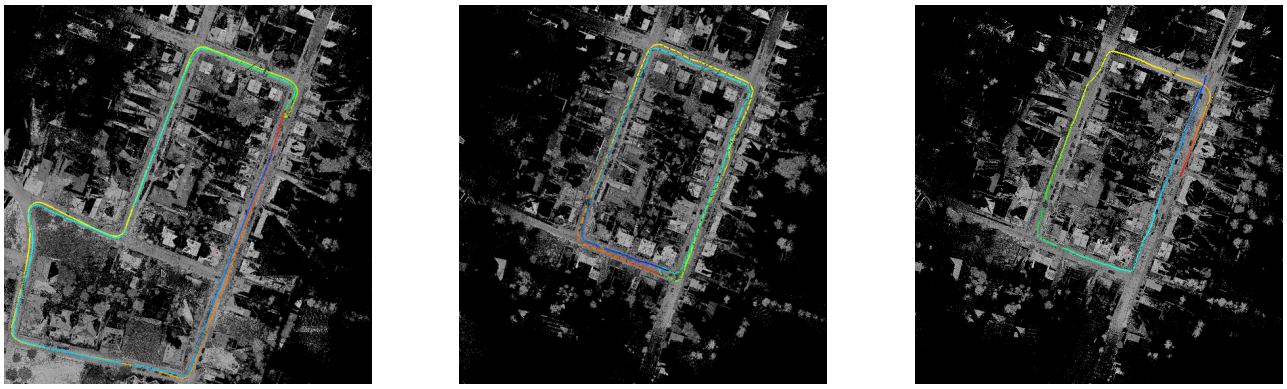

(a) VZ-600i on car roof. (b) VZ-600i on cargo bike. (c) VZ-600i on backpack.

Figure 11: Trajectories of the three kinematic data acquisitions (colored by time) overlaid on the corresponding point cloud (colored by reflectance).

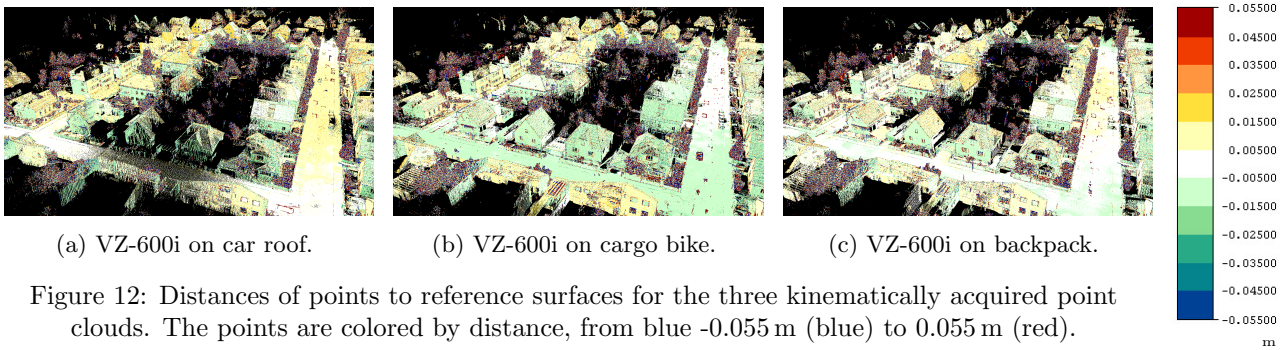

(a) VZ-600i on car roof. (b) VZ-600i on cargo bike. (c) VZ-600i on backpack.

Figure 12: Distances of points to reference surfaces for the three kinematically acquired point clouds. The points are colored by distance, from blue -0.055 m (blue) to 0.055 m (red).

Dataset	MIN_0	RMSE_0^{100}	MAX^{100}	$\mathrm{MIN}_{2.5}$	$\mathrm{RMSE}_{2.5}^{97.5}$	$\mathrm{MAX}^{97.5}$	MIN_5	RMSE_5^{95}	MAX^{95}
Car	-0.2495	0.0358	0.2495	-0.0857	0.0211	0.0862	-0.0523	0.0146	0.0520
Bike	-0.2495	0.0287	0.2498	-0.0635	0.0142	0.0655	-0.0318	0.0094	0.0312
On-foot	-0.2498	0.0332	0.2498	-0.0805	0.0187	0.0817	-0.0483	0.0119	0.0477

Table 1: Distances of kinematically acquired points w.r.t. the reference data best-fit planar surfaces using a 0.25 m voxelization. The minimum, root mean square error, and maximum of the distances are given for all data, as well as for robust subsets with the bottom/top 2.5% and respectively 5% cut off.

Dataset	MIN_0	SD_0^{100}	MAX^{100}	$\mathrm{MIN}_{2.5}$	$\mathrm{SD}_{2.5}^{97.5}$	$\mathrm{MAX}^{97.5}$	MIN_5	SD_5^{95}	MAX^{95}
Car	-0.2495	0.0244	0.2498	-0.0395	0.0073	0.0448	-0.0153	0.0041	0.0162
Bike	-0.2495	0.0239	0.2495	-0.0362	0.0064	0.0413	-0.0130	0.0034	0.0143
On foot	-0.2495	0.0254	0.2495	-0.0395	0.0074	0.0480	-0.0145	0.0041	0.0168

Table 2: Distances of kinematically acquired points w.r.t. the internal best-fit planar surfaces using a 0.25 m voxelization. The minimum, standard deviation and maximum of the distances are given for all data, as well as for robust subsets with the bottom/top 2.5% and respectively 5% cut off.

To evaluate the precision of the kinematic data, a similar procedure is used. Instead of reference surfaces from reference data, the kinematic dataset itself is used as a basis. Then, all points' distances to their respective nearest best-fit plane are computed, with minimum (MIN), standard deviation (SD), and maximum (MAX) shown in Table 2. In a manual evaluation of the building facades in the test datasets, the standard deviation of point normal distances from a best fit plane is consistently below 4 mm for all datasets, which matches the 5/95 percentile standard deviation shown above.

Additionally, we consider an extension of the classic stop-and-go laser scanning workflow. In a stop-and-go acquisition, the laser scanner is mounted on a motorized platform but data acquisition is performed only while the platform is static. The kinematic mapping mode enabled by our proposed methodology may also be used to augment such a stop-and-go workflow. Instead of only acquiring data during the *stop*-phase, additional data may be acquired during the *go*-phase. Fig. 13 shows the kinematically acquired point cloud (reflectance, grayscale) overlaid with the statically acquired scan (in magenta). This approach has two benefits: On the one hand, the static point cloud, considered more accurate, may be used to constrain the kinematic point cloud and thereby aid in the trajectory estimation. On the other hand, the addition of kinematically acquired points results in a denser and more detailed final point cloud and helps to fill in missing data where objects are occluded and not visible from the static scan positions.

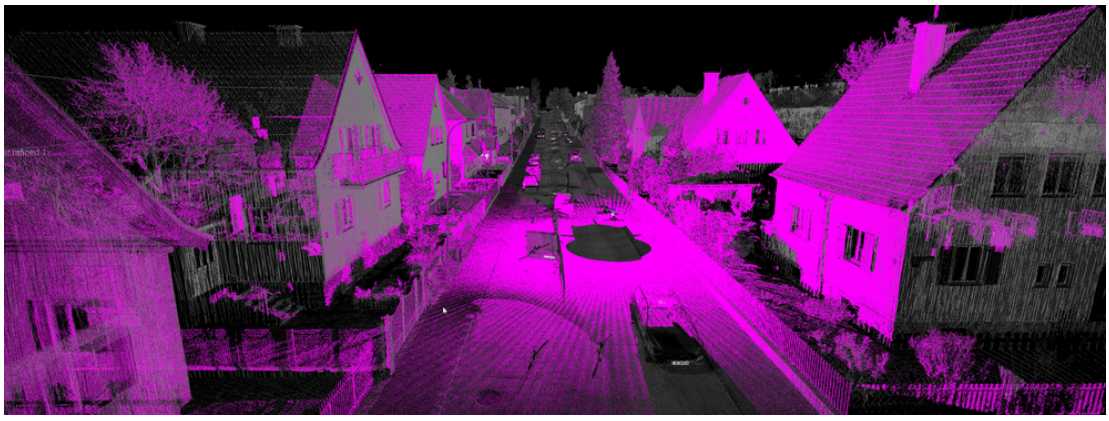

Figure 13: Static scan (magenta) augmented with kinematic scan (reflectance, grayscale).

4. CONCLUSION AND OUTLOOK

In this contribution, we presented a GNSS/IMU/LiDAR-based sensor fusion method for mobile mapping applications. Specifically, we show that this method allows the use of a survey-grade 3D terrestrial laser scanner for kinematic mapping, even though the internal IMU is orders of magnitude cheaper than what is commonly used in survey-grade mobile mapping systems. By comparison with statically acquired reference data we demonstrate a maximum RMSE of 3.6 cm (non-robust statistics) and 1.5 cm (robust statistics). On planar surfaces, the precision of the kinematically acquired point cloud is consistently better than $\sigma = 5$ mm.

More work is needed in order to explain the remaining systematic discrepancies visible between the TLS reference data and KLS data. This could be done for example by comparing to even more accurate reference data, acquired independently by different measurement techniques. A possible source of the remaining errors is the GNSS positioning. The sensor fusion architecture is currently based a loose coupling with the on-board RTK-GNSS, which depends on the presence of a sufficiently close base station as well as consistent signal reception for the RTK correction data. In future work, this limiting factor may be alleviated by employing post-processed or even tightly coupled GNSS.

ACKNOWLEDGMENTS

This work was carried out as part of the project ZAP-ALS (883660) funded by the Austrian Research Promotion Agency (FFG[†]).

REFERENCES

[1] Wang, Y., Chen, Q., Zhu, Q., Liu, L., Li, C., and Zheng, D., "A Survey of Mobile Laser Scanning Applications and Key Techniques over Urban Areas," *Remote Sensing* **11**(13) (2019).

[2] Schaer, P. and Vallet, J., "Trajectory Adjustment of Mobile Laser Scan Data in GPS Denied Environments," *ISPRS - International Archives of the Photogrammetry, Remote Sensing and Spatial Information Sciences* **XL-3/W4**, 61–64 (Mar. 2016).

[3] Pöppl, F., Neuner, H., Mandlburger, G., and Pfeifer, N., "Integrated Trajectory Estimation for 3D Kinematic Mapping with GNSS, INS and Imaging Sensors: A Framework and Review," *ISPRS Journal of Photogrammetry and Remote Sensing* **196**, 287–305 (Feb. 2023).

[4] Pöppl, F., Pfennigbauer, M., Ullrich, A., Mandlburger, G., Neuner, H., and Pfeifer, N., "Modelling of GNSS Positioning Errors in a GNSS/INS/LiDAR-integrated Georeferencing," *Publikationen der Deutschen Gesellschaft für Photogrammetrie, Fernerkundung und Geoinformation e.V.* (3. Wissenschaftlich-Technische Jahrestagung der DGPF), 183–196 (2023).

[5] Cadena, C., Carlone, L., Carrillo, H., Latif, Y., Scaramuzza, D., Neira, J., Reid, I., and Leonard, J. J., "Past, Present, and Future of Simultaneous Localization And Mapping: Towards the Robust-Perception Age," *IEEE Transactions on Robotics* **32**, 1309–1332 (Dec. 2016).

[6] Kim, M.-J., Kim, M.-S., and Shin, S. Y., "A General Construction Scheme for Unit Quaternion Curves with Simple High Order Derivatives," in [*Proceedings of the 22nd Annual Conference on Computer Graphics and Interactive Techniques - SIGGRAPH '95*], 369–376, ACM Press (1995).

[7] Farrell, J. A., Silva, F. O., Rahman, F., and Wendel, J., "Inertial Measurement Unit Error Modeling Tutorial: Inertial Navigation System State Estimation with Real-Time Sensor Calibration," *IEEE Control Systems* **42**, 40–66 (Dec. 2022).

[8] Groves, P. D., [*Principles of GNSS, Inertial, and Multisensor Integrated Navigation Systems*], GNSS Technology and Application Series, Artech House, Boston, 2nd ed. ed. (2013).

[9] Nurunnabi, A., West, G., and Belton, D., "Outlier Detection and Robust Normal-Curvature Estimation in Mobile Laser Scanning 3D Point Cloud Data," *Pattern Recognition* **48**, 1404–1419 (Apr. 2015).

[10] Savage, P. G., "Improved Strapdown Inertial Measurement Unit Calibration Procedures," in [*2018 IEEE/ION Position, Location and Navigation Symposium (PLANS)*], 522–533, IEEE, Monterey, CA (Apr. 2018).

[†]Österreichische Forschungsförderungsgesellschaft, Vienna, Austria, www.ffg.at